

Magnetoelastic coupling and effects of uniaxial strain in α -RuCl₃ from first principles

D. A. S. Kaib,^{1,*} S. Biswas,¹ K. Riedl,¹ S. M. Winter,^{1,2} and Roser Valentí¹

¹*Institut für Theoretische Physik, Goethe-Universität Frankfurt, Max-von-Laue-Strasse 1, 60438 Frankfurt am Main, Germany*

²*Department of Physics and Center for Functional Materials, Wake Forest University, Winston-Salem, North Carolina 27109, United States*

(Dated: August 9, 2022)

We present first-principles results on the magnetoelastic coupling in α -RuCl₃ and uncover a striking dependence of the magnetic coupling constants on strain effects. Different magnetic interactions are found to respond very unequally to variations in the lattice, with the Kitaev interaction being the most sensitive. Exact diagonalization results on our magnetoelastic model reproduce recent measurements of the structural Grüneisen parameter and explain the origin of the negative magnetostriction of α -RuCl₃, disentangling contributions related to different anisotropic interactions and g factors. Uniaxial strain perpendicular to the honeycomb planes is predicted to reorganize the relative coupling strengths, strongly enhancing the Kitaev interaction while simultaneously weakening the other anisotropic exchanges under compression. Uniaxial strain may therefore pose a fruitful route to experimentally tune α -RuCl₃ nearer to the Kitaev limit.

The exactly solvable Kitaev honeycomb model [1] features a quantum spin liquid (QSL) with non-Abelian anyons under magnetic fields. Following the proposal to realize the Kitaev interaction in real materials through an intricate exchange mechanism [2], so-called “Kitaev-candidate materials” emerged [3–6]. These are spin-orbit Mott insulators, whose low-energy magnetic degrees of freedom can be described through $j_{\text{eff}} = 1/2$ pseudospins. So far, most candidate materials exhibit long-range ordered magnetic ground states [7–12] instead of the Kitaev QSL due to residual extended interactions beyond the pure Kitaev model [12–17]. Nevertheless, the physics of such extended Kitaev models have led to countless interesting unconventional phenomena in these materials with arguably the most prominent example being α -RuCl₃. With the goal of tuning away from its antiferromagnetic zigzag order and possibly to a Kitaev QSL, various routes have been considered, including chemical doping [18–20], graphene substrates [21–24], hydrostatic pressure [25–29] and magnetic fields [30–36]. In the case of hydrostatic pressure, dimerization quickly destroys the $j_{\text{eff}} = 1/2$ picture [25, 29] such that no Kitaev QSL can occur. α -RuCl₃ under magnetic fields has however attracted great attention, due to the observation of a narrow field-induced regime of quantized thermal Hall conductivity in some samples [33, 35, 36]. Subsequent theoretical studies highlighted the importance of magnetoelastic coupling for the description of the thermal Hall conductivity [37, 38] and investigated further consequences of pseudospin-lattice-coupling [39, 40], in both cases for the idealized pure Kitaev model. However, realistic modeling, taking the actual lattice of α -RuCl₃ and its extended (non-Kitaev) interactions into account, is currently lacking. Recent works on Sr₂IrO₄ [41, 42] have demonstrated that magnetoelastic coupling can be crucial in understanding spin-orbit entangled j_{eff} materials.

In this work we explore the effects of *uniaxial* strain perpendicular to the honeycomb planes [Fig. 1] onto the

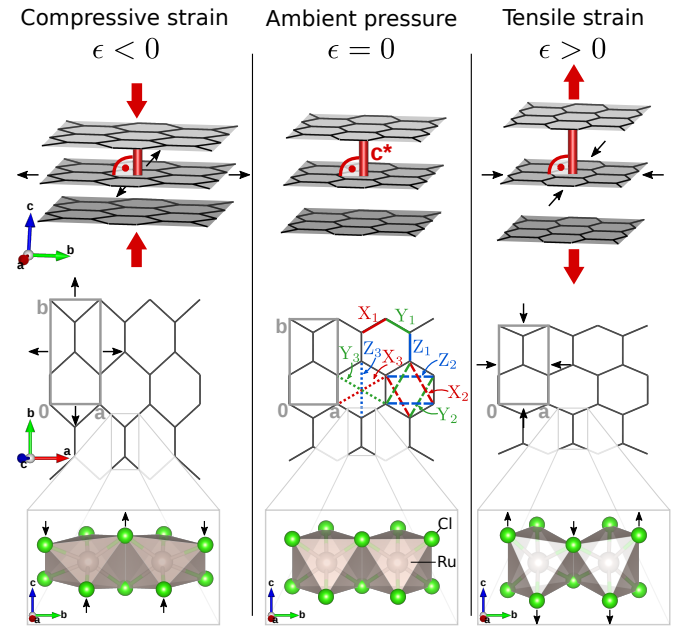


FIG. 1. Structural effects as a consequence of compressive [left column] and tensile [right column] uniaxial strain onto c^* . The middle column shows the unstrained structure. Enforced strains are indicated by red arrows and predicted responses of the system by black arrows. Shown from top to bottom are: Honeycomb layers, view onto one layer, and Ru-Ru bond with chlorine environment.

extended interactions in α -RuCl₃. By combining first-principles simulations and exact diagonalization we unveil a subtle dependence of the magnetic coupling constants on strain effects and provide a microscopic understanding of magnetoelastic properties in α -RuCl₃.

Magnetoelastic model.— We first derive the magnetoelastic Hamiltonian of α -RuCl₃ under a magnetic field \mathbf{B}

with uniaxial strain $\epsilon \equiv \Delta c^*/c_0^*$ as a degree of freedom,

$$\mathcal{H} = \sum_{ij} \mathbf{S}_i \cdot \mathbb{J}_{ij}(\epsilon) \cdot \mathbf{S}_j - \mu_B \sum_i \mathbf{B} \cdot \mathbb{G}(\epsilon) \cdot \mathbf{S}_i. \quad (1)$$

\mathbf{S}_i are $j_{\text{eff}} = 1/2$ operators and the strain-dependent tensors $\mathbb{J}_{ij}(\epsilon)$ and $\mathbb{G}(\epsilon)$ contain all exchange and g -tensor couplings. Our primary objective is then to extract the strengths of the linear magnetoelastic couplings $\tilde{\mathcal{J}} \equiv (\partial \mathcal{J} / \partial \epsilon)|_{\epsilon=0}$ for all components $\mathcal{J} \in \mathbb{J}_{ij}$ and $\mathcal{J} \in \mathbb{G}$. This way we (i) explore uniaxial strain as a potential tuning parameter in future experiments and (ii) enable theoretical modeling of observables that directly couple magnetic and structural degrees of freedom. We then apply our obtained magnetoelastic model to the field-dependent structural Grüneisen parameter and magnetostriction, finding excellent agreement with recent measurements [43].

For Kitaev materials the interaction tensor \mathbb{J}_{ij} is highly anisotropic and bond-directional-dependent. Bond types called X_n, Y_n and Z_n are defined on n th-nearest neighbors as shown in the center of Fig. 1. The exchange is then

$$\mathbb{J}_{ij} = \begin{pmatrix} \alpha & \beta & \gamma \\ \alpha & J_n & \Gamma_n + D_n^\gamma & \Gamma_n + D_n^\beta \\ \beta & \Gamma_n - D_n^\gamma & J_n & \Gamma_n + D_n^\alpha \\ \gamma & \Gamma_n - D_n^\beta & \Gamma_n - D_n^\alpha & J_n + K_n \end{pmatrix}, \quad (2)$$

where $(\alpha, \beta, \gamma) = (y, z, x)$ for X_n -bonds, (z, x, y) for Y_n , and (x, y, z) for Z_n -bonds. When K_1 is the only finite coupling, the model reduces to the exactly solvable Kitaev model [1]. The Dzyaloshinskii-Moriya interaction ($D_n^\alpha, D_n^\beta, D_n^\gamma$) vanishes for $n = 1, 3$ due to inversion symmetry. For simplicity we employ C_3 -symmetrized models throughout this manuscript, such that coupling strengths on X_n -, Y_n - and Z_n -bonds are equal for a given n . The computed non-symmetrized models are given in the Supplemental Material [44].

First-principles methods.— We investigate the effect of c^* -axis strain on the structure via constrained geometric optimizations. To obtain a zero-strain starting structure, the ambient-pressure experimental $C2/m$ structure [45] was fully relaxed, including all lattice parameters and atomic positions. Subsequently, the lattice parameters a, b , monoclinic angle β , and atomic positions were relaxed while constraining c to different values. For each obtained structure, the strain is then $\epsilon = \Delta c^*/c_0^*$, with $c^* = c \sin \beta$ and c_0^* denoting the unstrained parameter. The constrained relaxations were performed within GGA+ U [44, 46] in zigzag antiferromagnetic configurations using Quantum Espresso [47].

To determine the strain-dependent g -tensor components, we computed \mathbb{G} for each relaxed geometry on $[\text{RuCl}_6]^{3-}$ molecules with the quantum chemistry ORCA 3.03 package [48, 49] at the TPSSh/def2-TZVP/CAS(5,5) level, an approach that has proved reliable for isolated d^5 molecules [50].

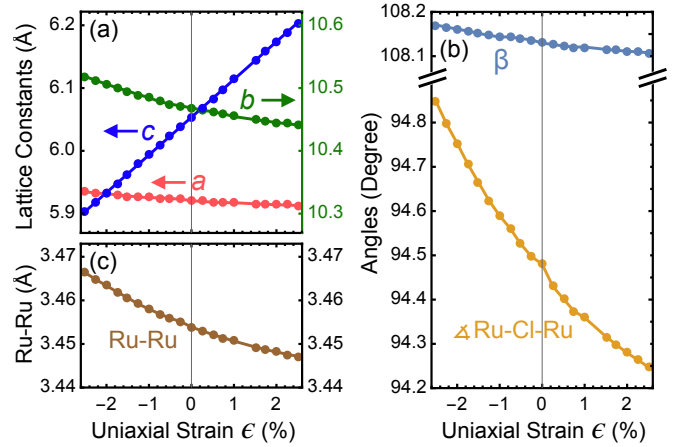


FIG. 2. Relaxed lattice parameters as a function of uniaxial strain on c^* . (a) Lattice constants. b is to be read with the right axis. (b) Monoclinic angle β and angle of the Ru-Cl-Ru bonds. (c) Average Ru-Ru bond length.

For the exchange interactions $\mathbb{J}_{ij}(\epsilon)$, we first computed non-relativistic hopping parameters for each relaxed structure in non-spin-polarized configurations within GGA using Full Potential Local Orbital (FPLO) code [51]. Magnetic interactions were then estimated via exact diagonalization (ED) of the two-site five-orbital Hubbard Hamiltonian and projection of the low-energy states onto the $j_{\text{eff}} = 1/2$ subspace [52, 53]. Here, we considered both t_{2g} and e_g orbitals explicitly, extending on previous approaches of some of the authors [53]. Further details on the methods are given in the Supplemental Material [44].

First-principles results.— The predicted effects of compressive (negative) and tensile (positive) uniaxial strain on the structure are summarized in Fig. 1 (showing illustrative extreme strains). Quantitative results are shown in Fig. 2. Upon compression along c^* , the honeycomb ab plane expands, increasing the Ru-Ru distance. Importantly, the octahedral chlorine environment, whose precise geometry mainly governs the Jackeli-Khaliulin exchange mechanism [2, 4, 54], is distorted in a strongly non-homogeneous way under uniaxial strain, see bottom row of Fig. 1.

The magnetoelastic couplings $\tilde{\mathcal{J}} \equiv (\partial \mathcal{J} / \partial \epsilon)|_{\epsilon=0}$ for each g -value ($\mathcal{J} \in \mathbb{G}$) and magnetic coupling parameter ($\mathcal{J} \in \mathbb{J}_{ij}$) were determined by differentiating third-order polynomial fits to their strain-dependencies as illustrated exemplary in Fig. 3(a,b) for the couplings with the strongest strain-dependence. Corresponding magnetoelastic couplings of the g values and nearest-neighbor interactions are compared in Fig. 3(c). The complete set of obtained ambient-pressure model parameters $\mathcal{J}|_{\epsilon=0}$ and $\tilde{\mathcal{J}}$ is listed in Table I.

The gyromagnetic tensor \mathbb{G} of each magnetic site is determined mainly by its local chlorine environment. Due to the non-trivial distortion under uniaxial strain ϵ

	g_{ab}	g_{c^*}	J_1	K_1	Γ_1	Γ'_1	J_2	K_2	Γ_2	Γ'_2	D_2^α	D_2^β	D_2^γ	J_3	K_3	Γ_3	Γ'_3
$\mathcal{J} _{\epsilon=0}$	2.36	1.88	-5.66	-10.12	9.35	-0.73	0.01	-0.18	0.06	0.03	0.02	0.04	0.07	0.2	0.25	0.04	-0.07
$\tilde{\mathcal{J}}$	-1.6	3.85	1.11	40.65	7.7	-11.34	-0.88	1.59	-0.44	-0.09	-1.2	-0.84	-3.14	1.62	0.55	-0.58	-0.46

TABLE I. C_3 -symmetrized magnetic couplings at ambient pressure $\mathcal{J}|_{\epsilon=0}$ and the associated magnetoelastic couplings $\tilde{\mathcal{J}} \equiv (\partial\mathcal{J}/\partial\epsilon)|_{\epsilon=0}$. Except for unitless g -tensor components, units are in meV. Strongest couplings are highlighted.

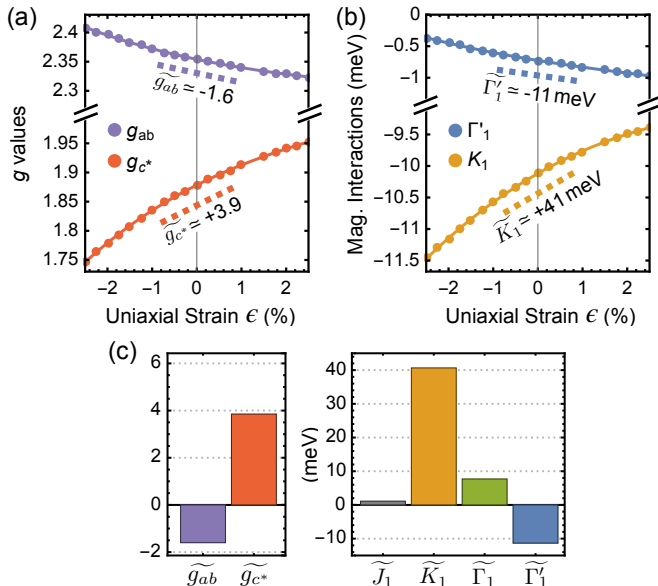


FIG. 3. (a) Calculated strain-dependence of g values and (b) K_1 , Γ'_1 (colored bullets). Solid curves show third-order polynomial fits. Dashed lines indicate $\tilde{\mathcal{J}} \equiv (\partial\mathcal{J}/\partial\epsilon)|_{\epsilon=0}$. (c) Comparison of magnetoelastic couplings $\tilde{\mathcal{J}}$ for g values and nearest-neighbor interactions.

[Fig. 1], the strain-dependence of the g -anisotropy cannot be explained with regular expressions [55] that are valid for trigonally compressed octahedral environments. From *ab-initio* we obtain for the zero-strain structure non-negligible components of \mathbb{G} : $g_{ab} = 2.36$ (in-plane) and $g_{c^*} = 1.88$ (out-of-plane), which fall in the range of existing estimates [55–58]. For their magnetoelastic couplings, we extract $\tilde{g}_{ab} = -1.6$ and $\tilde{g}_{c^*} = 3.85$. Compressive strain $\epsilon < 0$ will therefore increase g_{ab} and decrease g_{c^*} , enhancing the g anisotropy further, see Fig. 3(a).

The magnetic interactions \mathbb{J}_{ij} are mainly influenced by the corresponding Ru-Ru distances and the Ru-Cl-Ru geometry [Fig. 2(b,c)], influencing the orbital overlap integrals and with that the magnetic exchange between sites. Inclusion of virtual processes involving the e_g orbitals is found to strongly renormalize some interactions [44], doubling, for example, the magnitude of the Kitaev exchange K_1 . This interaction constitutes the strongest coupling in the ambient-strain model ($K_1 = -10.12$ meV) and has the strongest strain dependence ($\tilde{K}_1 = 40.65$ meV), see Fig. 3(c). The fact that the large \tilde{K}_1 has opposite sign of K_1 implies that *compressive* strain ($\epsilon < 0$) firmly

strengthens the Kitaev interaction. Regarding the results on the set of extended interactions as a whole, we emphasize that uniaxial strain affects different interactions unequally, strengthening some while weakening others — in contrast to effects predicted for volumetric strain or hydrostatic pressure [28]. Inspecting again the effect of compressive c^* -strain, the shared sign of $\tilde{\Gamma}_1$ with Γ_1 implies that $|\Gamma_1|$ will be *weakened*, which analogously holds for $|\Gamma'_1|$. The structure of the largest magnetoelastic couplings [bold in second row of Table I] therefore implies that compressive c^* -strain predominantly shifts interaction strength away from these anisotropic couplings and towards the Kitaev exchange K_1 .

Discussion.— For the application of our derived models we first focus on primarily magnetic observables. These are determined mainly by the zero-strain interactions $\mathcal{J}|_{\epsilon=0}$ [first row in Table I] and can be computed using ED in the projected $j_{\text{eff}} = 1/2$ basis on 24 sites [44]. Throughout, we find very good agreement with experimental observations. In particular, the zigzag-ordered ground state, correct critical field strengths [30, 59] and the evolution of the magnetic torque [60–62] and magnetotropic coefficient [61, 63] are captured. Peculiarly, a ferromagnetic phase is highly proximate to the ground state, and zigzag order is only upheld by the weak $\Gamma'_1 = -0.73$ meV. The large $\tilde{\Gamma}'_1 = -11.34$ meV therefore implies that compressive c^* -strain should strongly destabilize zigzag order. Detailed results for magnetic properties are shown in the Supplemental Material [44].

Our main focus lies on *magnetoelastic* properties, which are driven by $\tilde{\mathcal{J}}$. Motivated by recent measurements by Gass *et al.* [43], we concentrate on linear magnetostriction $\lambda_{c^*} \equiv c^{*-1}(\partial c^*/\partial B)$ and the structural Grüneisen parameter $\Gamma_s \equiv -\frac{(\partial S_m/\partial p_{c^*})}{T(\partial S_m/\partial T)}$. Here p_{c^*} is uniaxial pressure along c^* and S_m the magnetic entropy, which the authors of Ref. 43 obtained via subtraction of phononic contributions. Under the assumption that the diagonal components of the elasticity tensor are dominant, the observables can be approximated [44]

$$\lambda_{c^*} \approx \frac{\kappa_{c^*c^*}}{V} \sum_{\mathcal{J} \in \mathbb{J}_{ij}, \mathbb{G}} \tilde{\mathcal{J}} \left(\frac{\partial M}{\partial \mathcal{J}} \right)_{\epsilon=0}, \quad (3)$$

$$\Gamma_s \approx \frac{\kappa_{c^*c^*}}{T} \sum_{\mathcal{J} \in \mathbb{J}_{ij}, \mathbb{G}} \tilde{\mathcal{J}} \left(\frac{\partial S_m}{\partial \mathcal{J}} \right)_{\epsilon=0} \left(\frac{\partial S_m}{\partial T} \right)_{\epsilon=0}^{-1}, \quad (4)$$

where the sums go over all strain-dependent interactions and g values: $\mathcal{J} \in \{J_1, K_1, \dots, g_{ab}, g_{c^*}\}$. The magneto-

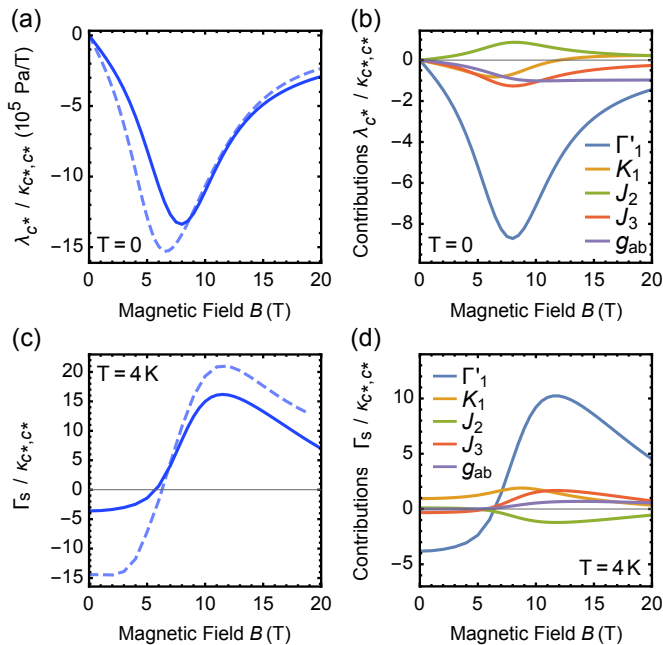


FIG. 4. (a) Calculated field-dependent magnetostriction at $T = 0$ and (c) structural Grüneisen parameter at $T = 4$ K. (b,d) Dissection of the largest contributions to the respective quantities via Eqs. (3) and (4). Solid lines: Obtained using all $\tilde{\mathcal{J}}$ and $\mathcal{J}|_{\epsilon=0}$ from Table I. Dashed lines: Obtained using all $\tilde{\mathcal{J}}$ from Table I and $\mathcal{J}|_{\epsilon=0}$ from the model of Ref. 64.

elastic couplings $\tilde{\mathcal{J}}$ are taken from Table I and the derivatives are evaluated at $\epsilon = 0$ (i.e., at parameters $\mathcal{J}|_{\epsilon=0}$) within ED. We compute quantities up to the unknown $\kappa_{c^*c^*} \equiv -(\partial\epsilon/\partial p_{c^*})$ of α -RuCl₃, defined as the linear compressibility along c^* against *uniaxial* pressure p_{c^*} .

In Fig. 4 we present results for λ_{c^*} and Γ_s obtained from the Table I parameters as solid curves (dashed curves are discussed below). Fig. 4(a) shows the $T \rightarrow 0$ magnetostriction λ_{c^*} as a function of in-plane field $\mathbf{B} \parallel b$. The magnetostriction exhibits its maximum magnitude at the critical field of the model ($B_c \approx 7.5$ T). Note that finite-size effects in ED typically broaden features near the critical field, hence λ_{c^*} is expected to peak sharper at B_c in the thermodynamic limit [44]. For increasing field strengths $B > B_c$, the magnitude of λ_{c^*} shrinks monotonically. The *negative* magnetostriction throughout implies a field-induced compression of α -RuCl₃. We therefore find very good agreement with experiment [43], although it is not clear whether a subtle reported kink above B_c [43] is also present in our results.

In order to extract more information out of these results, it is useful to dissect individual contributions to the magnetostriction, $\tilde{\mathcal{J}} \cdot (\partial M/\partial \mathcal{J})$, stemming from the interplay of different interactions \mathcal{J} with the lattice. One may expect that the magnetostriction would be influenced strongly by the summand with $\mathcal{J} = K_1$ due to the large \tilde{K}_1 (cf. Fig. 3(c)). However, we find the associated

magnetization susceptibility ($\partial M/\partial K_1$) to be negligible in magnitude compared to other magnetization susceptibilities. Instead, the magnetostriction is found to be governed by the summand with $\mathcal{J} = \Gamma'_1$, as shown in Fig. 4(b). Here $(\partial M/\partial \Gamma'_1) > 0$, which can already be anticipated on the classical level [44], and $\tilde{\Gamma}'_1 < 0$. The negative magnetostriction may therefore be understood as follows: Under increased B , α -RuCl₃ can lower its Zeeman energy further (i.e., increase its magnetization) by *increasing* $\tilde{\Gamma}'_1$ ($\partial M/\partial \tilde{\Gamma}'_1 > 0$), which is achieved by c^* -compression ($\tilde{\Gamma}'_1 < 0$).

We now turn to the structural Grüneisen parameter Γ_s , computed via Eq. (4) and ED. Here, we achieve finite temperatures by restricting the canonical sums to the lowest 16 eigenstates, which works well for lowest temperatures [44]. Results are shown in Fig. 4(c,d). We again find a good qualitative agreement with experiment [43], with a sign change from negative to positive near $B = B_c$. Likely because of finite-size effects, the slope at the sign change is not vertical, and Γ_s only reaches its maximum for fields slightly above B_c . In contrast to experiment, we obtain $|\Gamma_s(B \lesssim B_c)| < |\Gamma_s(B \gtrsim B_c)|$. Dissecting the contributions from different magnetoelastic couplings in Fig. 4(d), we again find that the contribution related to $\tilde{\Gamma}'_1$ dominates the magnetoelastic response. Analyzing our results for temperatures below that of the experiment (4 K), we predict most of the qualitative response to be unchanged. However, we note that our model also predicts an anomalous drop in both the structural (Γ_s) and magnetic (Γ_B) Grüneisen parameters at high fields $B > 20$ T [44, 65], which becomes increasingly sharp at lower temperatures. Experimentally, such an anomaly was clearly observed in Γ_B around $B \approx 10$ T at $T < 2$ K [65], and is also suggested by recent data on Γ_s at $T = 3.5$ K in the same field range [43]. These anomalies are understood to occur due to interchange of lowest excited states [65], which occurs at a field strength that is sensitive to the specific couplings. This may be considered for future refinements of the model.

In the results discussed so far, we employed the complete set of magnetic interactions $\mathcal{J}|_{\epsilon=0}$ and magnetoelastic couplings $\tilde{\mathcal{J}}$ from Table I. However, our results on the magnetoelastic coupling may also provide guidelines for theoretical modeling in reduced parameter spaces. Therefore we also considered a *minimal* magnetic model $\{\mathcal{J}|_{\epsilon=0}\}$ with only four nonzero interactions, $(J_1, K_1, \Gamma_1, J_3) = (-0.5, -5.0, 2.5, 0.5)$ meV and $g_{ab} = 2.3$, which has reproduced key experimental observations on magnetic properties [57–59, 64–67]. We repeated our calculations, evaluating the derivatives in Eqs. (3) and (4) at these minimal-model values $\mathcal{J}|_{\epsilon=0}$ (keeping the magnetoelastic couplings $\tilde{\mathcal{J}}$ from Table I). Results are shown as dashed lines in Fig. 4(a,c). Overall, the results are comparable to before. Note—importantly—that a summand in Eqs. (3) and (4) related to $\tilde{\mathcal{J}}$ is *not* required to

vanish if the respective $\mathcal{J}|_{\epsilon=0}$ is zero. On the contrary, we find also in the case of this minimal model that contributions from the magnetoelastic coupling $\widetilde{\Gamma}'_1$ essentially dominate the response, regardless of $\Gamma'_1|_{\epsilon=0} = 0$. This highlights that the dominant magnetoelastic interactions in α -RuCl₃ can be of completely different form than the dominant ambient-pressure magnetic interactions.

Considering the strongest $\widetilde{\mathcal{J}}$ [bold in Table I], a “minimal set of magnetoelastic couplings” may consist of $\widetilde{K}_1, \widetilde{\Gamma}_1, \widetilde{\Gamma}'_1$. However, since Γ'_1 controls the stability of the zigzag phase the strongest, effects related to $\widetilde{\Gamma}'_1$ are likely to be prominent in many magnetoelastic effects, as found in those studied here. Note, though, that with increasingly high field strengths, \widetilde{g}_{ab} (and \widetilde{g}_{c^*} for out-of-plane fields) gains importance.

Conclusions.— We derived a magnetoelastic Hamiltonian for α -RuCl₃ completely from *ab-initio*. We have shown that it reproduces key magnetic phenomena of α -RuCl₃ and can explain recent field-dependent structural Grüneisen and magnetostriction measurements [43]. For magnetoelastic properties, a Γ'_1 -type magnetoelastic coupling (“ $\widetilde{\Gamma}'_1$ ”) is found to dominate, albeit the associated interaction Γ'_1 being subdominant in the purely magnetic part of the Hamiltonian. Compressive uniaxial strain perpendicular to the honeycomb planes is predicted to strongly destabilize zigzag order while shifting interaction strength from other anisotropic couplings towards the Kitaev exchange. The strong reorganization of the magnetic interactions by uniaxial strain is a result of the geometry-sensitive exchange mechanisms in Kitaev materials and therefore likely extends also to other two- and three-dimensional Kitaev materials.

Acknowledgments.— We thank Anja Wolter and Bernd Büchner for fruitful discussions and we acknowledge the Deutsche Forschungsgemeinschaft (DFG, German Research Foundation) for funding through Project No. 411289067 (VA117/15-1) and TRR 288 — 422213477 (project A05).

* kaib@itp.uni-frankfurt.de

- [1] A. Kitaev, *Ann. Phys.* **321**, 2 (2006).
- [2] G. Jackeli and G. Khaliullin, *Phys. Rev. Lett.* **102**, 017205 (2009).
- [3] J. G. Rau, E. K.-H. Lee, and H.-Y. Kee, *Annu. Rev. Condens. Matter Phys.* **7**, 195 (2016).
- [4] S. M. Winter, A. A. Tsirlin, M. Daghofer, J. van den Brink, Y. Singh, P. Gegenwart, and R. Valentí, *J. Condens. Matter Phys.* **29**, 493002 (2017).
- [5] M. Hermanns, I. Kimchi, and J. Knolle, *Annu. Rev. Condens. Matter Phys.* **9**, 17 (2018).
- [6] H. Takagi, T. Takayama, G. Jackeli, G. Khaliullin, and S. E. Nagler, *Nat. Rev. Phys.* **1**, 264 (2019).
- [7] X. Liu, T. Berlijn, W.-G. Yin, W. Ku, A. Tsvelik, Y.-J. Kim, H. Gretarsson, Y. Singh, P. Gegenwart, and J. P. Hill, *Phys. Rev. B* **83**, 220403(R) (2011).
- [8] F. Ye, S. Chi, H. Cao, B. C. Chakoumakos, J. A. Fernandez-Baca, R. Custelcean, T. F. Qi, O. B. Korneta, and G. Cao, *Phys. Rev. B* **85**, 180403(R) (2012).
- [9] A. Biffin, R. D. Johnson, S. Choi, F. Freund, S. Manni, A. Bombardi, P. Manuel, P. Gegenwart, and R. Coldea, *Phys. Rev. B* **90**, 205116 (2014).
- [10] J. A. Sears, M. Songvilay, K. W. Plumb, J. P. Clancy, Y. Qiu, Y. Zhao, D. Parshall, and Y.-J. Kim, *Phys. Rev. B* **91**, 144420 (2015).
- [11] R. D. Johnson, S. C. Williams, A. A. Haghighirad, J. Singleton, V. Zapf, P. Manuel, I. I. Mazin, Y. Li, H. O. Jeschke, R. Valentí, and R. Coldea, *Phys. Rev. B* **92**, 235119 (2015).
- [12] S. C. Williams, R. D. Johnson, F. Freund, S. Choi, A. Jesche, I. Kimchi, S. Manni, A. Bombardi, P. Manuel, P. Gegenwart, and R. Coldea, *Phys. Rev. B* **93**, 195158 (2016).
- [13] J. Chaloupka, G. Jackeli, and G. Khaliullin, *Phys. Rev. Lett.* **105**, 027204 (2010).
- [14] J. Chaloupka, G. Jackeli, and G. Khaliullin, *Phys. Rev. Lett.* **110**, 097204 (2013).
- [15] J. G. Rau, E. K.-H. Lee, and H.-Y. Kee, *Phys. Rev. Lett.* **112**, 077204 (2014).
- [16] A. Biffin, R. D. Johnson, I. Kimchi, R. Morris, A. Bombardi, J. G. Analytis, A. Vishwanath, and R. Coldea, *Phys. Rev. Lett.* **113**, 197201 (2014).
- [17] E. K.-H. Lee and Y. B. Kim, *Phys. Rev. B* **91**, 064407 (2015).
- [18] A. Koitzsch, C. Habenicht, E. Müller, M. Knupfer, B. Büchner, S. Kretschmer, M. Richter, J. van den Brink, F. Börrnert, D. Nowak, A. Isaeva, and T. Doert, *Phys. Rev. Mater.* **1**, 052001(R) (2017).
- [19] G. Bastien, M. Roslova, M. H. Haghighi, K. Mehlawat, J. Hunger, A. Isaeva, T. Doert, M. Vojta, B. Büchner, and A. U. B. Wolter, *Phys. Rev. B* **99**, 214410 (2019).
- [20] S.-H. Baek, H. W. Yeo, S.-H. Do, K.-Y. Choi, L. Janssen, M. Vojta, and B. Büchner, *arXiv preprint arXiv:2005.13836* (2020).
- [21] S. Mashhadi, Y. Kim, J. Kim, D. Weber, T. Taniguchi, K. Watanabe, N. Park, B. Lotsch, J. H. Smet, M. Burghard, *et al.*, *Nano Letters* **19**, 4659 (2019).
- [22] B. Zhou, J. Balgley, P. Lampen-Kelley, J.-Q. Yan, D. Mandrus, and E. A. Henriksen, *Phys. Rev. B* **100**, 165426 (2019).
- [23] S. Biswas, Y. Li, S. M. Winter, J. Knolle, and R. Valentí, *Phys. Rev. Lett.* **123**, 237201 (2019).
- [24] E. Gerber, Y. Yao, T. A. Arias, and E.-A. Kim, *Phys. Rev. Lett.* **124**, 106804 (2020).
- [25] T. Biesner, S. Biswas, W. Li, Y. Saito, A. Pustogov, M. Altmeyer, A. U. B. Wolter, B. Büchner, M. Roslova, T. Doert, S. M. Winter, R. Valentí, and M. Dressel, *Phys. Rev. B* **97**, 220401(R) (2018).
- [26] G. Bastien, G. Garbarino, R. Yadav, F. J. Martinez-Casado, R. B. Rodríguez, Q. Stahl, M. Kusch, S. Lيماندي, R. Ray, P. Lampen-Kelley, *et al.*, *Phys. Rev. B* **97**, 241108(R) (2018).
- [27] Z. Wang, J. Guo, F. F. Tafti, A. Hegg, S. Sen, V. A. Sidorov, L. Wang, S. Cai, W. Yi, Y. Zhou, H. Wang, S. Zhang, K. Yang, A. Li, X. Li, Y. Li, J. Liu, Y. Shi, W. Ku, Q. Wu, R. J. Cava, and L. Sun, *Phys. Rev. B* **97**, 245149 (2018).
- [28] R. Yadav, S. Rachel, L. Hozoi, J. van den Brink, and G. Jackeli, *Phys. Rev. B* **98**, 121107(R) (2018).

- [29] G. Li, X. Chen, Y. Gan, F. Li, M. Yan, F. Ye, S. Pei, Y. Zhang, L. Wang, H. Su, *et al.*, *Phys. Rev. Mater.* **3**, 023601 (2019).
- [30] S.-H. Baek, S.-H. Do, K.-Y. Choi, Y. S. Kwon, A. U. B. Wolter, S. Nishimoto, J. van den Brink, and B. Büchner, *Phys. Rev. Lett.* **119**, 037201 (2017).
- [31] Z. Wang, S. Reschke, D. Hüvonen, S.-H. Do, K.-Y. Choi, M. Gensch, U. Nagel, T. Rõõm, and A. Loidl, *Phys. Rev. Lett.* **119**, 227202 (2017).
- [32] A. Banerjee, P. Lampen-Kelley, J. Knolle, C. Balz, A. A. Aczel, B. Winn, Y. Liu, D. Pajerowski, J. Yan, C. A. Bridges, A. T. Savici, B. C. Chakoumakos, M. D. Lumsden, D. A. Tennant, R. Moessner, D. G. Mandrus, and S. E. Nagler, *npj Quantum Mater.* **3**, 8 (2018).
- [33] Y. Kasahara, T. Ohnishi, Y. Mizukami, O. Tanaka, S. Ma, K. Sugii, N. Kurita, H. Tanaka, J. Nasu, Y. Motome, T. Shibauchi, and Y. Matsuda, *Nature* **559**, 227 (2018).
- [34] C. Balz, P. Lampen-Kelley, A. Banerjee, J. Yan, Z. Lu, X. Hu, S. M. Yadav, Y. Takano, Y. Liu, D. A. Tennant, M. D. Lumsden, D. Mandrus, and S. E. Nagler, *Phys. Rev. B* **100**, 060405(R) (2019).
- [35] T. Yokoi, S. Ma, Y. Kasahara, S. Kasahara, T. Shibauchi, N. Kurita, H. Tanaka, J. Nasu, Y. Motome, C. Hickey, *et al.*, arXiv preprint arXiv:2001.01899 (2020).
- [36] M. Yamashita, N. Kurita, and H. Tanaka, arXiv preprint arXiv:2005.00798 (2020).
- [37] Y. Vinkler-Aviv and A. Rosch, *Phys. Rev. X* **8**, 031032 (2018).
- [38] M. Ye, G. B. Halász, L. Savary, and L. Balents, *Phys. Rev. Lett.* **121**, 147201 (2018).
- [39] A. Metavitsiadis and W. Brenig, *Phys. Rev. B* **101**, 035103 (2020).
- [40] M. Ye, R. M. Fernandes, and N. B. Perkins, arXiv preprint arXiv:2002.05328 (2020).
- [41] H. Liu and G. Khaliullin, *Phys. Rev. Lett.* **122**, 057203 (2019).
- [42] J. Porras, J. Bertinshaw, H. Liu, G. Khaliullin, N. H. Sung, J.-W. Kim, S. Francoual, P. Steffens, G. Deng, M. M. Sala, A. Efimenko, A. Said, D. Casa, X. Huang, T. Gog, J. Kim, B. Keimer, and B. J. Kim, *Phys. Rev. B* **99**, 085125 (2019).
- [43] S. Gass, P. Cónsoli, V. Kocsis, L. Corredor, P. Lampen-Kelley, D. G. Mandrus, S. E. Nagler, L. Janssen, M. Vojta, B. Büchner, and A. U. B. Wolter, *Phys. Rev. B* **101**, 245158 (2020).
- [44] See Supplementary Material for technical details on *ab-initio* and ED methods, complete obtained *ab-initio* model parameters, ED results on primarily magnetic properties and derivation of Eqs. (3) and (4).
- [45] H. B. Cao, A. Banerjee, J.-Q. Yan, C. A. Bridges, M. D. Lumsden, D. G. Mandrus, D. A. Tennant, B. C. Chakoumakos, and S. E. Nagler, *Phys. Rev. B* **93**, 134423 (2016).
- [46] J. P. Perdew, K. Burke, and M. Ernzerhof, *Phys. Rev. Lett.* **77**, 3865 (1996).
- [47] P. Giannozzi, S. Baroni, N. Bonini, M. Calandra, R. Car, C. Cavazzoni, D. Ceresoli, G. L. Chiarotti, M. Cococcioni, I. Dabo, *et al.*, *J. Condens. Matter Phys.* **21**, 395502 (2009).
- [48] F. Neese, *Wiley Interdiscip. Rev. Comput. Mol. Sci.* **2**, 73 (2012).
- [49] F. Neese, *J. Chem. Phys.* **122**, 034107 (2005).
- [50] K. S. Pedersen, J. Bendix, A. Tressaud, E. Durand, H. Weihe, Z. Salman, T. J. Morsing, D. N. Woodruff, Y. Lan, W. Wernsdorfer, *et al.*, *Nat. Commun.* **7**, 1 (2016).
- [51] K. Koepernik and H. Eschrig, *Phys. Rev. B* **59**, 1743 (1999).
- [52] K. Riedl, Y. Li, R. Valentí, and S. M. Winter, *Phys. Status Solidi B* **256**, 1800684 (2019).
- [53] S. M. Winter, Y. Li, H. O. Jeschke, and R. Valentí, *Phys. Rev. B* **93**, 214431 (2016).
- [54] J. G. Rau and H.-Y. Kee, arXiv preprint arXiv:1408.4811 (2014).
- [55] J. Chaloupka and G. Khaliullin, *Phys. Rev. B* **94**, 064435 (2016).
- [56] R. Yadav, N. A. Bogdanov, V. M. Katukuri, S. Nishimoto, J. van den Brink, and L. Hozoi, *Sci. Rep.* **6**, 37925 (2016).
- [57] S. M. Winter, K. Riedl, D. Kaib, R. Colde, and R. Valentí, *Phys. Rev. Lett.* **120**, 077203 (2018).
- [58] A. Sahasrabudhe, D. A. S. Kaib, S. Reschke, R. German, T. C. Koethe, J. Buhot, D. Kamenskyi, C. Hickey, P. Becker, V. Tsurkan, A. Loidl, S. H. Do, K. Y. Choi, M. Grüninger, S. M. Winter, Z. Wang, R. Valentí, and P. H. M. van Loosdrecht, *Phys. Rev. B* **101**, 140410(R) (2020).
- [59] A. Wolter, L. Corredor, L. Janssen, K. Nenkov, S. Schönecker, S.-H. Do, K.-Y. Choi, R. Albrecht, J. Hunger, T. Doert, *et al.*, *Phys. Rev. B* **96**, 041405(R) (2017).
- [60] I. A. Leahy, C. A. Pocs, P. E. Siegfried, D. Graf, S.-H. Do, K.-Y. Choi, B. Normand, and M. Lee, *Phys. Rev. Lett.* **118**, 187203 (2017).
- [61] K. A. Modic, M. D. Bachmann, B. J. Ramshaw, F. Arnold, K. R. Shirer, A. Estry, J. B. Betts, N. J. Ghimire, E. D. Bauer, M. Schmidt, *et al.*, *Nat. Commun.* **9**, 1 (2018).
- [62] K. A. Modic, B. J. Ramshaw, A. Shekhter, and C. M. Varma, *Phys. Rev. B* **98**, 205110 (2018).
- [63] K. Modic, R. D. McDonald, J. Ruff, M. D. Bachmann, Y. Lai, J. C. Palmstrom, D. Graf, M. Chan, F. Balakirev, J. B. Betts, *et al.*, arXiv preprint arXiv:2005.04228 (2020).
- [64] S. M. Winter, K. Riedl, P. A. Maksimov, A. L. Chernyshev, A. Honecker, and R. Valentí, *Nat. Commun.* **8**, 1 (2017).
- [65] S. Bachus, D. Kaib, Y. Tokiwa, A. Jesche, V. Tsurkan, A. Loidl, S. Winter, A. Tsirlin, R. Valentí, and P. Gegenwart, arXiv preprint arXiv:2006.02428 (2020).
- [66] J. Cookmeyer and J. E. Moore, *Phys. Rev. B* **98**, 060412(R) (2018).
- [67] K. Riedl, Y. Li, S. M. Winter, and R. Valentí, *Phys. Rev. Lett.* **122**, 197202 (2019).
- [68] H. Suzuki, H. Liu, J. Bertinshaw, K. Ueda, H. Kim, S. Laha, D. Weber, Z. Yang, L. Wang, H. Takahashi, *et al.*, arXiv preprint arXiv:2008.02037 (2020).
- [69] S. Grimme, *J. Phys. Chem. Solids* **27**, 1787 (2006).
- [70] H. J. Monkhorst and J. D. Pack, *Phys. Rev. B* **13**, 5188 (1976).
- [71] G. Kresse and J. Hafner, *Phys. Rev. B* **47**, 558 (1993).
- [72] P. E. Blöchl, *Phys. Rev. B* **50**, 17953 (1994).
- [73] H.-S. Kim and H.-Y. Kee, *Phys. Rev. B* **93**, 155143 (2016).
- [74] V. Hermann, M. Altmeyer, J. Ebad-Allah, F. Freund, A. Jesche, A. A. Tsirlin, M. Hanfland, P. Gegenwart, I. I. Mazin, D. I. Khomskii, R. Valentí, and C. A. Kuntscher, *Phys. Rev. B* **97**, 020104 (2018).

- [75] V. Hermann, S. Biswas, J. Ebad-Allah, F. Freund, A. Jesche, A. A. Tsirlin, M. Hanfland, D. Khomskii, P. Gegenwart, R. Valentí, and C. A. Kuntscher, *Phys. Rev. B* **100**, 064105 (2019).
- [76] A. Banerjee, J. Yan, J. Knolle, C. A. Bridges, M. B. Stone, M. D. Lumsden, D. G. Mandrus, D. A. Tennant, R. Moessner, and S. E. Nagler, *Science* **356**, 1055 (2017).
- [77] S.-H. Do, S.-Y. Park, J. Yoshitake, J. Nasu, Y. Motome, Y. S. Kwon, D. T. Adroja, D. J. Voneshen, K. Kim, T.-H. Jang, J.-H. Park, K.-Y. Choi, and S. Ji, *Nat. Phys.* **13**, 1079 (2017).
- [78] P. Lampen-Kelley, L. Janssen, E. Andrade, S. Rachel, J.-Q. Yan, C. Balz, D. Mandrus, S. Nagler, and M. Vojta, arXiv preprint arXiv:1807.06192 (2018).
- [79] J. C. Slater, *Quantum theory of atomic structure*, Tech. Rep. (1960).
- [80] C. Eichstaedt, Y. Zhang, P. Laurell, S. Okamoto, A. G. Eguiluz, and T. Berlijn, *Phys. Rev. B* **100**, 075110 (2019).
- [81] K. Foyevtsova, H. O. Jeschke, I. I. Mazin, D. I. Khomskii, and R. Valentí, *Phys. Rev. B* **88**, 035107 (2013).
- [82] H.-S. Kim, V. V. Shankar, A. Catuneanu, and H.-Y. Kee, *Phys. Rev. B* **91**, 241110 (2015).
- [83] Y. S. Hou, H. J. Xiang, and X. G. Gong, *Phys. Rev. B* **96**, 054410 (2017).

Supplemental Material:

Magnetoelastic coupling and effects of uniaxial strain in α -RuCl₃ from first principles

Magnetic properties of the *ab-initio* derived model

We study primarily magnetic properties of the $\{\mathcal{J}|_{\epsilon=0}\}$ model given in Table I of the main text. While the physics of these properties have been covered and discussed in previous modeling, they provide comparisons to a wide array of measurements. Therefore the results presented in this section serve primarily as benchmark of our fully *ab-initio* obtained model and thus of the applied first-principles methodology. To compute different observables within the model, we employ ED in the $j_{\text{eff}} = 1/2$ basis on a hexagon-shaped 24-site cluster. We employ all 17 parameters of the main-text Table I model. Note that restricting to the nearest-neighbor couplings ($J_1, K_1, \Gamma_1, \Gamma'_1$) of this model gives similar results regarding zigzag order and critical field strengths within ED. But in the following we follow through with all parameters to consistently work with fully *ab-initio* results.

At $\mathbf{B} = 0, T = 0$, the model correctly reproduces anti-ferromagnetic zigzag order within ED, revealed by dominant static spin-spin correlations $\langle \mathbf{S}(-\mathbf{q}) \cdot \mathbf{S}(\mathbf{q}) \rangle$ at the zigzag ordering wave vectors $\mathbf{q} = M, M', Y$. However, significant ferromagnetic correlations $\langle \mathbf{S}(0) \cdot \mathbf{S}(0) \rangle \approx 0.7 \langle \mathbf{S}(-M) \cdot \mathbf{S}(M) \rangle$ are also persistent, as a result of the strong ferromagnetic $|J_1| \approx 0.5|K_1|$ in the model (Table I of the main text). This is consistent with the findings of a recent study using resonant inelastic X-ray scattering [68]. In the present model, ferromagnetism is so competitive, that the ferromagnetic state ($\mathbf{q} = 0$) is lower in energy than the zigzag one on the classical level. Zigzag order found in ED is therefore likely a result of significant quantum fluctuations. The small $\Gamma'_1 = -0.73$ meV [Table I in main text] stabilizes this order, and zigzag order is lost for $\Gamma'_1 \gtrsim -0.2$ meV (keeping all other interactions unchanged) within ED. Recalling the effects of compressive c^* -strain as discussed in the main text, *i.e.*, a strong suppression of $|\Gamma'_1|$ and $|\Gamma_1|$ together with a vast increase of $|K_1|$, we estimate compressive strains of $\epsilon \sim -3\%$ to -5% to be sufficient to suppress zigzag order (at zero field).

We now turn to properties at finite magnetic fields \mathbf{B} . Figure S1(a) shows the magnetization as a function of field strength for in-plane fields $\mathbf{B} \parallel b$ and out-of-plane fields $\mathbf{B} \parallel c^*$. These are compared to the experimental data of Ref. 11 at $T < 2$ K. We thus find good agreement. To probe for field-induced phase transitions of the model, we show in Fig. S1(b) the fidelity susceptibility $\chi_F = [2/(\delta B)^2][1 - \langle \Psi_0(B) | \Psi_0(B + \delta B) \rangle]$ and the second derivative of the ground state energy $(-\partial^2 E_0 / \partial B^2)$ for in-plane fields $\mathbf{B} \parallel b$. These reveal

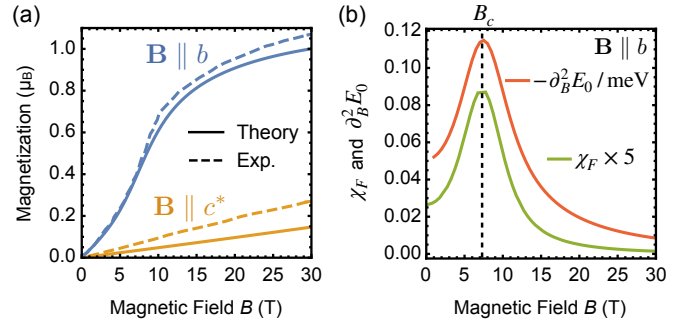


FIG. S1. Field-strength-dependent ED results on the model $\{\mathcal{J}|_{\epsilon=0}\}$ of Table I in the main text. (a) Magnetization for $\mathbf{B} \parallel b$ (in-plane) and $\mathbf{B} \parallel c^*$ (out-of-plane). Dashed curves show experimental data from Ref. 11. (b) Second derivative of the ground-state energy and fidelity susceptibility χ_F .

a single phase transition as a function of field strength at $B_c \approx 7.5$ T, between the low-field zigzag ordered phase and the high-field partially-polarized phase. The critical field for the perpendicular direction within the honeycomb plane ($\mathbf{B} \parallel a$) is found to be similar, while zigzag order is much more stable for fields perpendicular to the plane ($\mathbf{B} \parallel c^*$) with $B_c \approx 82$ T. These results are all consistent with experiment, and the physics are analogous to those described in the context of a minimal model in Ref. 57.

In Fig. S2(a) we show the field-angle-dependent magnetic torque $\tau \equiv dE/d\theta$ as a function of the out-of-plane angle θ . $\theta = 0$ corresponds to the in-plane direction b and $\theta = 90^\circ$ to the out-of-plane direction c^* . The essential evolution with field-angle and field-strength and the characteristic sawtooth-shape reproduce the experiments [60–62] well. Fig. S2(b) shows the magnetotropic coefficient $k \equiv d\tau/d\theta$, which is also in good qualitative agreement with experiment [61, 63]. The physics of τ and k within the present model are analogous to those described in detail in Ref. 67.

Derivation of Equations (3) and (4) of the main text

We derive Eqs. (3) and (4) of the main text. These were used to estimate the field-dependent magnetostriction $\lambda_{c^*} \equiv L_{c^*}^{-1}(\partial L_{c^*} / \partial B) = \partial \epsilon / \partial B$ and the structural Grüneisen parameter $\Gamma_s \equiv -\frac{(\partial S_m / \partial p_{c^*})}{T(\partial S_m / \partial T)}$. Here, L_{c^*} is the length of the crystal along c^* , S_m the magnetic entropy and p_{c^*} uniaxial pressure along c^* . We start with the general expression of the change in the Gibbs free energy under consideration of anisotropic strain and stress

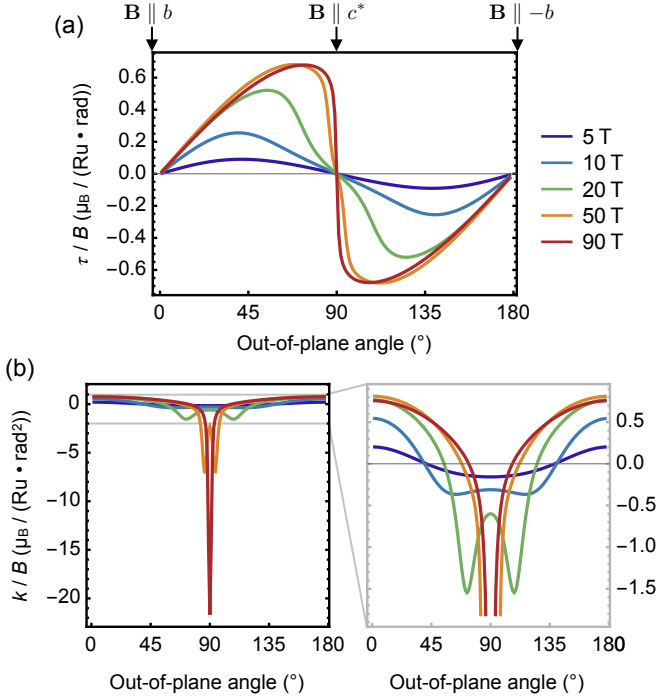


FIG. S2. Field-angle-dependent ED results on the model $\{\mathcal{J}|_{\epsilon=0}\}$ of Table I in the main text. The field-direction rotates from b (in-plane) over c^* (out-of-plane) to $-b$. (a) Magnetic torque normalized by field strength, $\tau/B = (dE/d\theta)/B$. (b) Normalized magnetotropic coefficient $k/B = (d\tau/d\theta)/B$. The lower-right panel shows a narrower plot range for k/B .

contributions

$$d\mathcal{G} = \sum_{ij} \epsilon_{ij} d\sigma_{ij} - S dT - M dB, \quad (\text{S1})$$

with the strain tensor ϵ_{ij} , the stress tensor σ_{ij} and the crystallographic indices $i, j \in \{a, b, c^*\}$. Note that throughout the manuscript we have used the shorthand notation $\epsilon_{c^*c^*} \equiv \epsilon$ for uniaxial strain onto c^* . Equation (S1) implies a Maxwell relation for the magnetostriction

$$\lambda_{c^*} = \left(\frac{\partial \epsilon_{c^*c^*}}{\partial B} \right)_{T, \{\sigma_{ij}\}} = \left(\frac{\partial M}{\partial \sigma_{c^*c^*}} \right)_{T, B, \{\sigma_{ij}\} \setminus \{\sigma_{c^*c^*}\}}. \quad (\text{S2})$$

Here, the subscript $\{\sigma_{ij}\}$ denotes that all stress-components are held constant, while $\{\sigma_{ij}\} \setminus \{\sigma_{c^*c^*}\}$ holds all strains except $\sigma_{c^*c^*}$ constant.

The right-hand side of Eq. (S2) can also be expressed through the elasticity tensor c_{ijkl} , which connects the strain and stress tensors through

$$\sigma_{ij} = \sum_{kl} c_{ijkl} \epsilon_{kl}. \quad (\text{S3})$$

Then, we have with Eqs. (S2) and (S3):

$$\left(\frac{\partial M}{\partial \sigma_{c^*c^*}} \right)_X = \sum_{ij} \left[c_{c^*c^*ij} \left(\frac{\partial \epsilon_{ij}}{\partial M} \right)_X \right]^{-1}, \quad (\text{S4})$$

where the variables $X = (T, B, \{\sigma_{ij}\} \setminus \{\sigma_{c^*c^*}\})$ are held constant in the derivatives.

We now employ the assumption that the elasticity contribution along the direction of the investigated length change ΔL_{c^*} is dominant, i.e., $c_{c^*c^*c^*c^*} \gg c_{c^*c^*ij}$ for $i, j \neq c^*$. Then we can approximate the magnetostriction as

$$\lambda_{c^*} \approx \frac{\kappa_{c^*c^*}}{V} \left(\frac{\partial M}{\partial \epsilon_{c^*c^*}} \right)_X, \quad (\text{S5})$$

where we expressed $c_{c^*c^*c^*c^*}$ through the linear compressibility under uniaxial pressure $\kappa_{c^*c^*} = -\frac{\partial \epsilon_{c^*c^*}}{\partial p_{c^*}} = -V \frac{\partial \epsilon_{c^*c^*}}{\partial \sigma_{c^*c^*}} = -V c_{c^*c^*c^*c^*}^{-1}$. Note that the derivative in Eq. (S5) does importantly *not* hold the other lattice constants a, b or the atom positions constant. Instead these degrees of freedom need to be evolved to their new equilibrium positions when $\epsilon_{c^*c^*}$ is varied, i.e., the structure needs to be relaxed under constrained variations of $\epsilon_{c^*c^*}$, as we have done.

In Eq. (S5), a change in $\epsilon_{c^*c^*}$ affects the magnetization M through the variation of the magnetic interactions \mathbb{J}_{ij} and of the g -tensor \mathbb{G} of the pseudospins. This can be expressed formally by applying the chain rule on Eq. (S5), which leads to

$$\lambda_{c^*} \approx \frac{\kappa_{c^*c^*}}{V} \sum_{\mathcal{J} \in \mathbb{J}_{ij}, \mathbb{G}} \left[\left(\frac{\partial M}{\partial \mathcal{J}} \right) \left(\frac{\partial \mathcal{J}}{\partial \epsilon_{c^*c^*}} \right) \right]_X, \quad (\text{S6})$$

Since the compressibility $\kappa_{c^*c^*}$ of α -RuCl₃ is not known, we can not predict the absolute change in $\epsilon_{c^*c^*}$ under magnetic field, but instead compute $\lambda_{c^*}/\kappa_{c^*c^*}$. We thus have to evaluate the derivatives in Eq. (S6) at $\epsilon_{c^*c^*} = 0$. While this is an approximation at finite fields, we note that the total integrated field-induced change of $\epsilon_{c^*c^*}$ is below 0.1% at $B = 15$ T [43], despite α -RuCl₃ having a comparatively large magnetostriction effect. The influence of such small field-induced changes in $\epsilon_{c^*c^*}$ onto the field-dependence on the contributions in Eq. (S6) is therefore negligible, cf. Figs. S6 and S7. Instead, the main dependence on magnetic field in Eq. (S6) is expected to be carried by the field-dependent derivative containing the magnetization M . With the definition $\tilde{\mathcal{J}} \equiv (\partial \mathcal{J} / \partial \epsilon_{c^*c^*})|_{\epsilon_{c^*c^*}=0}$ we thus arrive at

$$\lambda_{c^*} \approx \frac{\kappa_{c^*c^*}}{V} \sum_{\mathcal{J} \in \mathbb{J}_{ij}, \mathbb{G}} \tilde{\mathcal{J}} \left(\frac{\partial M}{\partial \mathcal{J}} \right)_{X, \epsilon_{c^*c^*}=0}, \quad (\text{S7})$$

which coincides with Eq. (3) of the main text.

For the structural Grüneisen parameter $\Gamma_s \equiv -\frac{\partial S_m / \partial \sigma_{c^*c^*}}{VT(\partial S_m / \partial T)}$, an analogous approach can be made, where in Eq. (S4) M is replaced with S_m . Analogously one arrives at

$$\Gamma_s \approx \frac{\kappa_{c^*c^*}}{T} \sum_{\mathcal{J} \in \mathbb{J}_{ij}, \mathbb{G}} \tilde{\mathcal{J}} \left(\frac{\partial S_m}{\partial \mathcal{J}} \right)_{\epsilon_{c^*c^*}=0} \left(\frac{\partial S_m}{\partial T} \right)_{\epsilon_{c^*c^*}=0}^{-1}, \quad (\text{S8})$$

which coincides with Eq. (4) of the main text.

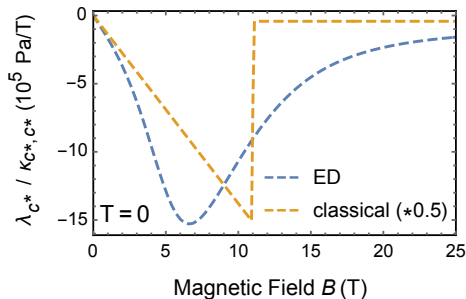


FIG. S3. Comparison of ED and classical results for the field-dependent magnetostriction of the minimal magnetic model $\{\mathcal{J}|_{\epsilon=0}\}$ of Ref. 64 in conjunction with our magnetoelastic couplings $\tilde{\mathcal{J}}$ from main-text Table I. Classical result is divided by a factor of 2.

Classical results for magnetostriction in the minimal model

The results presented in Fig. 4 of the main text are affected by finite-size effects of the 24-site ED calculations. To show that the peak of the magnetostriction at $B = B_c$ likely becomes sharper in the thermodynamic limit, we compare to a classical calculation of the $T = 0$ magnetostriction, that is free of finite-size effects. Here, the magnetization susceptibilities $(\partial M / \partial \mathcal{J})$ in Eq. (S7) are evaluated by classical energy minimization of the minimal magnetic model $\{\mathcal{J}|_{\epsilon=0}\}$ of Ref. 64 while the magnetoelastic couplings $\tilde{\mathcal{J}}$ are taken from Table I (main text). An analogous classical calculation is not possible on the full *ab-initio*-derived model of Table I (main text) as that model does not have a zigzag ground state on the classical level, but the insights likely apply also to that model.

Results are shown in Fig. S3. Note that the classical result is divided by a factor of 2 for better comparability. Aside from the increased overall magnitude compared to the ED result, the drop of $|\lambda_{c^*}|$ is much more pronounced here, which is more consistent with experiment. A smearing-out of phase transitions is expected as a typical finite-size effect. However, the classical result lacks the quantum fluctuations that are present in ED, such that the critical field strength is overestimated ($B_{c,\text{classical}} = 11$ T, $B_{c,\text{ED}} = 6$ T).

Both in the classical and in the ED results, we note that the dominating contribution to λ_{c^*} comes from the summand in Eq. (S7) that described magnetoelastic coupling to $\tilde{\mathcal{J}}$. An increase in Γ'_1 lowers the critical field, such that —within the zigzag phase $B < B_c$ — spins are stronger canted towards the direction of the magnetic field for a given field strength B , i.e., have higher magnetization. Therefore, $(\partial M / \partial \Gamma'_1 > 0)$, which together with $\tilde{\Gamma}'_1 < 0$ [Table I (main text)] explains an overall *negative* sign of the magnetostriction.

Details on structural Grüneisen parameter

The structural Grüneisen parameter $\Gamma_s \equiv -\frac{(\partial S_m / \partial p_{c^*})}{T(\partial S_m / \partial T)}$ can not be obtained from a pure ground state calculation (where the entropy would vanish). As we are interested in low-but-finite temperature calculations, we employ a method where we restrict the canonical sums to the lowest d_c eigenstates,

$$Z \approx \sum_{n=0}^{d_c-1} e^{-E_n / (k_B T)},$$

$$\langle O \rangle \approx \frac{1}{Z} \sum_{n=0}^{d_c-1} e^{-E_n / (k_B T)} \langle n | O | n \rangle, \quad (\text{S9})$$

which has proven reliable for calculations of the magnetic Grüneisen parameter Γ_B [65]. We use Eq. (S9) to evaluate the structural Grüneisen parameter at $T = 4$ K via Eq. (S8) and ED with up to $d_c = 16$. The dependence on d_c of our results is shown in Fig. S4(b), which corresponds for $d_c = 16$ to the unbroken line in Fig. 4(c) of the main text. As these results are very robust already for $d_c > 3$, we deem the results very reliable. In Fig. S4(d) we show the error analysis for the case where the minimal magnetic model of Ref. 64 is used for the $\mathcal{J}|_{\epsilon=0}$ couplings. Here, results appear not fully converged at $T = 4$ K, but we assume trends to be correct. This can also be seen at the exact $T = 0$ result shown in Fig. S4(c) of the same model. Here an exact evaluation is possible as the $T \rightarrow 0$ limit of a Grüneisen parameter is only determined by the behavior of the gap between the ground state and lowest excited state [65].

Inspecting the zero-temperature limit of Γ_s in our full *ab-initio* model from the main-text Table I, shown in Fig. S4(a), a discontinuity is apparent at $B = 22.5$ T. This is the result of a level crossing in the first two excited states at this field strength, which produces such an anomaly in all Grüneisen parameters of the form $\Gamma_\lambda \equiv -\frac{\partial S / \partial \lambda}{T(\partial S / \partial T)}$ [65]. At small finite temperatures [blue curve in Fig. S4(a)], the discontinuity is smeared out to a shoulderlike feature, and is mostly invisible for intermediate and high temperatures, as in Fig. S4(b) for $T = 4$ K. An analogous shoulder-anomaly has been observed experimentally in the *magnetic* Grüneisen parameter Γ_B at $B \sim 10$ T, that resembles the anomaly in Γ_B in our model [65]. While the location of the shoulder-anomalies in this model and experiment appear far apart, we note that —up to our knowledge— no other realistic model proposed so far for α -RuCl₃ (including the minimal model [64] we discussed) features any such shoulder-anomaly in Grüneisen parameters. In the present model, level crossing between the lowest excited states, that produces the shoulder-anomaly, happens between the zigzag ordering wave vector and $\mathbf{k} = 0$. We interpret this as a result of the strongly competing ferromagnetic phase (with ordering wave vector $\mathbf{q} = 0$) in the present model. As the

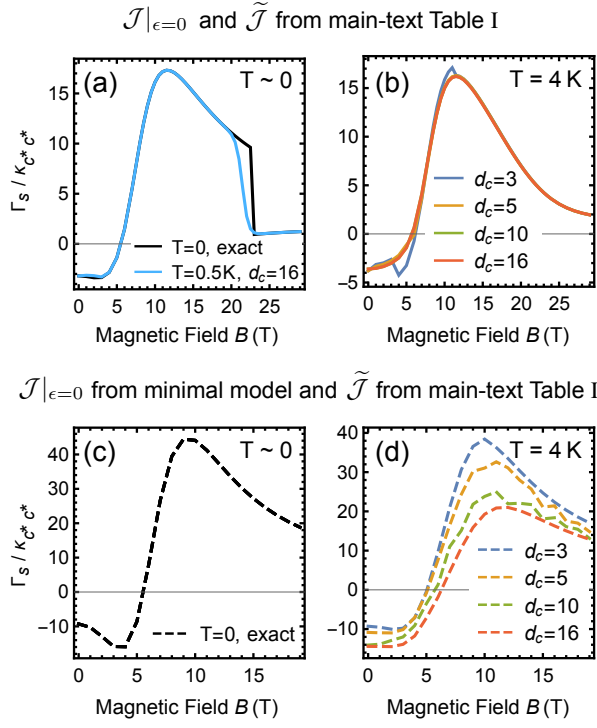


FIG. S4. Detailed results on temperature-dependence and estimation of the cutoff errors for the structural Grüneisen parameter Γ_s . Top panels (a,b) show results for $\mathcal{J}|_{\epsilon=0}$ and $\tilde{\mathcal{J}}$ from main-text Table I, bottom panels (c,d) show results for $J|_{\epsilon=0}$ from the minimal magnetic model of Ref. 64 and $\tilde{\mathcal{J}}$ from main-text Table I. (a,c) Zero and low-temperature results. (b,d) Results at $T = 4$ K for different employed cutoffs d_c (see Eq. (S9)).

precise field strength at which the anomaly appears is highly sensitive to the coupling strengths, future refinements of the model may take this into account.

Further Details of First-principles Calculations

Structural relaxation.— The constrained relaxations were performed using *ab-initio* DFT as implemented in the QUANTUM ESPRESSO (QE) package [47] in zigzag antiferromagnetic configurations of ruthenium. A plane-wave basis set was used to expand the electronic wave functions and the exchange-correlation functional was approximated by the generalized gradient approximation (GGA+ U) of Perdew, Burke, and Ernzerhof [46] with $U = 1.5$ eV. The cutoff for the plane-wave basis set and the cutoff for the corresponding charge densities were set at 60 and 600 Ry, respectively. We considered Van-der-Waals corrections within Grimme’s DFT-D2 method [69]. A Monkhorst-Pack [70] grid of size $8 \times 6 \times 8$ was used to generate the k-mesh (zone centered) for the corresponding Brillouin-zone sampling.

In order to check the effects of spin-orbit coupling

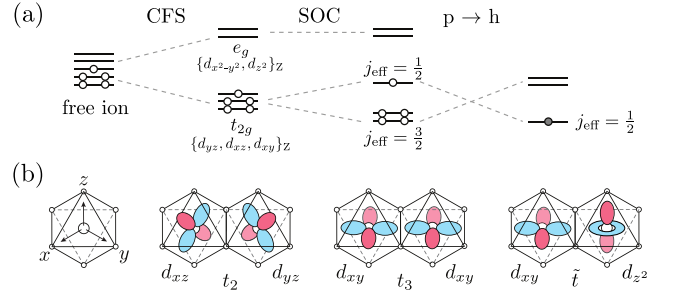


FIG. S5. (a) Effects of crystal field splitting (CFS), spin-orbit coupling (SOC) and a particle-hole ($p \rightarrow h$) transformation in a d^5 configuration. (b) Dominant hopping processes t_2 , t_3 and \tilde{t} on the Z-bond for the experimental structure of α -RuCl $_3$, explicitly given in Eq. (S10).

(SOC) on the relaxation, we used VASP code [71] using the projector-augmented plane-wave basis [72]. For this, the unstrained structural optimization at ambient pressure was recalculated with VASP in the GGA+ U approximation and the results from the two methods were found to agree well. Then the former code was used to find the effect of SOC (within GGA+ U +SOC) on the lattice geometry. We find that SOC mainly brings the structure further to approximate C_3 symmetry of the honeycomb planes. This effect is in line with other studies of honeycomb ruthenates, iridates and rhodates [73–75] and consistent with the approximately C_3 -symmetric magnetic response observed in α -RuCl $_3$ [11, 76–78]. These observations also vindicate our work with a C_3 -simplified version of the obtained magnetic model throughout the discussions in the main text.

Exchange interaction calculations.— With the structural response toward uniaxial strain ϵ established, each structure can be associated with a magnetic Hamiltonian determined by \mathbb{J}_{ij} and \mathbb{G} (see Eq. (1) of the main text). To extract the corresponding coupling parameters $\mathcal{J} \in \mathbb{J}_{ij}$, we first construct the multi-orbital Hubbard Hamiltonian for the ruthenium sites.

For the two-particle interaction terms, we used spherically symmetric expressions [79], parameterized by Slater integrals, and fixing them to values based on recent cRPA results for α -RuCl $_3$ [80]. The local two-particle exchange parameters were obtained by subtraction of the non-local contributions given in Ref. 80. Averaging over the orbital-dependent expression and taking an effective two-particle on-site interaction lead then to the parameters employed in this work, $U_{t_{2g}} = F_0 + (4/49)(F_2 + F_4) = 2.58$ eV and $J_{t_{2g}} = (3/49)F_2 + (20/441)F_4 = 0.29$ eV.

The material-specific properties are encoded in the first-principles ruthenium hopping parameters. As illustrated in Fig. S5(a), the crystal field splitting (CFS) due to the octahedral chlorine environment causes a splitting between energetically low t_{2g} orbitals and the higher in energy e_g orbitals. Due to the energy gap the low-

energy properties of the system can be described in terms of a low-spin configuration, where the electrons populate the t_{2g} orbitals. Spin-orbit coupling (SOC) was included in the atomic approximation with a SOC parameter $\lambda = 0.15$ eV [53]. Considering such strong spin-orbit coupling, the t_{2g} orbitals form together with the spin 1/2 degree of freedom $j_{\text{eff}} = 1/2$ and $j_{\text{eff}} = 3/2$ states [see Fig. S5(a)]. Since the $j_{\text{eff}} = 3/2$ states are fully occupied, exact diagonalization of the two-site five-orbital Hubbard Hamiltonian allows then to project the determined low-energy states onto a bilinear pseudospin 1/2 Hamiltonian. The resulting bond-resolved first-principles coupling parameters up to third nearest neighbors at $\epsilon = 0$ are shown in Table SI. C_3 -symmetrization of these values lead to the parameters given in the main text.

As uniaxial strain along c^* affects the distance between the honeycomb planes stronger than in-plane distances (see Fig. 2 of the main text), one might expect magnetoelastic couplings related to inter-plane couplings to be significant. We have estimated their magnetoelastic couplings with the same procedures as given here, and found that they are on the order of $\tilde{\mathcal{J}} \sim 1$ meV, while the nearest-neighbor in-plane magnetoelastic couplings are on the order of $\tilde{\mathcal{J}} \sim 10$ meV. Inter-plane couplings have therefore been neglected in the further discussion of this study.

Effects of e_g orbitals

Although the nearest neighbor Kitaev interaction was introduced within the three-orbital t_{2g} framework of the Khaliullin-Jackeli mechanism [2, 4, 54], the role of e_g orbitals for Kitaev materials was previously considered in some approximations [14, 81, 82]. In this work, we extended the approach by some of the authors [53], where the Hubbard Hamiltonian was constructed with only t_{2g} ruthenium orbitals. Interestingly, inclusion of the e_g orbitals leads to an increase of the magnitudes of the g tensor components as well as the bilinear magnetic interactions, given in Table SI, including the ferromagnetic nearest-neighbor Kitaev interaction K_1 . Meanwhile, the magnetoelastic couplings are in most cases overestimated if e_g effects are neglected.

If only t_{2g} orbitals were considered, the relevant Hilbert space could be reduced by a particle-hole transformation, which results in a projection of the one-hole low-energy solution onto pseudospin 1/2 operators [see Fig. S5(a)]. Additional consideration of e_g orbitals within this procedure takes higher-order hopping processes into account that lead to corrections of the final effective pseudospin Hamiltonian. The present analysis is limited to two-site clusters, which likely leads to underestimation of second and third neighbor couplings, which were found to be of non-negligible magnitude [53, 83]. However, this restriction is necessary to limit computational expense.

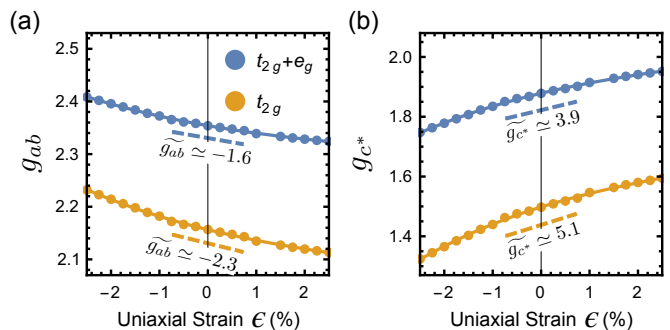


FIG. S6. g -values at different uniaxial strains ϵ , either taking into account only the t_{2g} orbitals [CAS(5,3)] or all five d -orbitals [$t_{2g} + e_g$; CAS(5,5)]. Solid lines show third-order polynomial fits. Values next to the dashed lines indicate $\tilde{\mathcal{J}} \equiv (\partial J / \partial \epsilon)|_{\epsilon=0}$.

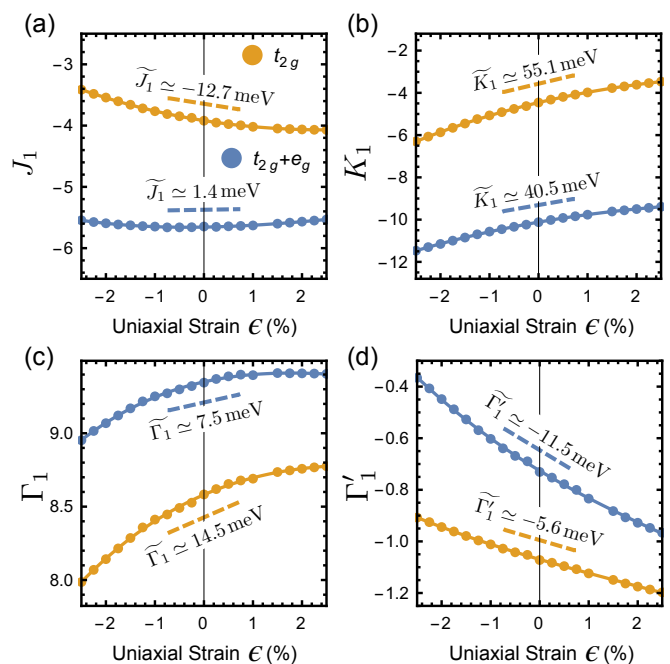


FIG. S7. Nearest-neighbor magnetic interactions at different uniaxial strains ϵ , either taking account for only the t_{2g} orbitals or all five d -orbitals ($t_{2g} + e_g$). Solid lines show third-order polynomial fits. Values next to the dashed lines indicate $\tilde{\mathcal{J}} \equiv (\partial J / \partial \epsilon)|_{\epsilon=0}$.

In order to highlight the effects of the e_g orbitals on the g -tensor, we compare the results obtained from ORCA [48] at the CASSCF/TPSSH/def2-TZVP level on RuCl_6^{3-} clusters, using active space definitions of (5,3) and (5,5). The former explicitly excludes any configurations with partial occupancy of the e_g orbitals, while the latter includes those configurations. In both cases, we considered equal weight on all doublet states in the orbital optimization. The e_g effects for the C_3 -symmetrized g tensor components as a function of uniaxial strain ϵ are illustrated in Fig. S6. At $\epsilon = 0$, the full approach consid-

	g_a	g_b	g_{c^*}	J_1	K_1	Γ_1	Γ'_1	J_2	K_2	Γ_2	Γ'_2	D_2^α	D_2^β	D_2^γ	J_3	K_3	Γ_3	Γ'_3
$\mathcal{J}_{5\text{orb}}^Z$	2.27	2.44	1.88	-4.99	-12.38	6.85	-1.15	0.02	-0.09	0.04	-0.04	0.03	0.03	0.17	0.31	0.23	0.07	-0.05
$\mathcal{J}_{5\text{orb}}^X$				-6.00	-8.99	10.6	-0.51	0.00	-0.22	0.07	0.06	0.01	0.05	0.01	0.15	0.26	0.24	-0.08
$\mathcal{J}_{3\text{orb}}^Z$	2.07	2.25	1.50	-2.43	-7.66	5.45	-1.43	-0.29	-0.60	0.06	-0.15	-0.02	-0.02	0.03	0.30	0.26	-0.09	-0.13
$\mathcal{J}_{3\text{orb}}^X$				-4.67	-2.86	10.14	-0.89	-0.78	0.49	-0.14	0.1	-0.07	0.06	-0.05	0.09	0.31	-0.18	-0.17

TABLE SI. g -tensor components and magnetic interactions $\mathcal{J}^Z|_{\epsilon=0}$ ($\mathcal{J}^X|_{\epsilon=0}$) on Z-bonds (X-bonds) in meV for the zero-strain relaxed $C2/m$ structure before C_3 symmetrization and with hopping parameters considering all five Ru $4d$ orbitals ($\mathcal{J}_{5\text{orb}}$) compared to only Ru t_{2g} orbitals ($\mathcal{J}_{3\text{orb}}$).

ering ($t_{2g} + e_g$) orbitals reveals an increased magnitude for both, g_{ab} and g_{c^*} . This increase is not homogeneous, leading to a reduction of the anisotropy g_{ab}/g_{c^*} . Considering the non-symmetrized values in Table SI, it also becomes evident that the anisotropy within the honeycomb plane, i.e., $g_a < g_b$, is reduced by e_g effects. The magnetoelastic couplings \widetilde{g}_{ab} and \widetilde{g}_{c^*} are reduced upon consideration of these effects, so that an overestimation of the coupling to the lattice can be prevented by consideration of such higher order processes.

In Fig. S7 we compare strain-dependent nearest neighbor magnetic interactions considering t_{2g} and ($t_{2g} + e_g$) orbitals. In this case, e_g effects can be related to the first-principles hopping parameters between them and the low-energy t_{2g} orbitals. For the $\epsilon = 0$ structure we computed the following parameters on the Z-bond (the bond parallel to the b direction, see Fig. 1 of the main text):

$$t_Z = \begin{pmatrix} & d_{yz} & d_{xz} & d_{xy} & d_{x^2-y^2} & d_{z^2} \\ d_{yz} & +0.04 & +\mathbf{0.15} & -0.01 & 0 & 0 \\ d_{xz} & +\mathbf{0.15} & +0.04 & -0.01 & 0 & 0 \\ d_{xy} & -0.01 & -0.01 & -\mathbf{0.08} & 0 & +\mathbf{0.28} \\ d_{x^2-y^2} & 0 & 0 & 0 & -0.01 & 0 \\ d_{z^2} & 0 & 0 & +\mathbf{0.28} & 0 & 0 \end{pmatrix} \quad (\text{S10})$$

The highlighted dominant hopping mechanisms are illustrated in Fig. S5(b). While t_2 and t_3 are strong hoppings

within the t_{2g} orbitals, we find the strongest hopping to be \tilde{t} , which connects the t_{2g} orbital d_{xy} with the e_g orbital d_{z^2} .

Consideration of this additional large exchange mechanism leads to a reshuffling of relative coupling strengths with an overall tendency to an increase in magnitude (see also Table SI). The only reduced nearest neighbor interaction is Γ'_1 .

The magnetoelastic couplings $\widetilde{\mathcal{J}}$, illustrated by the slope of the dashed lines in Fig. S7, of most interaction parameters follow the same trend, but become reduced in magnitude upon consideration of e_g orbitals. $\widetilde{\mathcal{J}}_1$ shows the only sign-change [Fig. S7(a)], where with $\widetilde{\mathcal{J}}_1 = -12.7$ meV a negative contribution is vastly overestimated in the three-orbital case compared to the (positive) five-orbital result of $\widetilde{\mathcal{J}}_1 = 1.4$ meV. Another change in trend shows $\widetilde{\Gamma}'_1$ [Fig. S7(d)], where the magnetoelastic coupling is underestimated with $\widetilde{\Gamma}'_1 = -5.32$ meV, compared to the five-orbital result $\widetilde{\Gamma}'_1 = -11.34$ meV. Hence, in order to appreciate the important coupling to the lattice of this interaction parameter, consideration of all five orbitals is crucial.

We therefore conclude that the interplay of higher order hopping processes together with the structure of Hund's coupling in d block elements lead to a delicate coupling between magnetism and structure that — to the best of our knowledge — has not been captured with analytical methods such as perturbation theory so far.